Precision Orbit of δ Delphini and Prospects for Astrometric Detection of Exoplanets

Tyler Gardner[1] , John D. Monnier[1] , Francis C. Fekel[2] , Mike Williamson[2], Douglas K. Duncan[3], Timothy R. White[4] ,
Michael Ireland[5] , Fred C. Adams[6] , Travis Barman[7], Fabien Baron[8] , Theo ten Brummelaar[9], Xiao Che[1],
Daniel Huber[10,11,12] , Stefan Kraus[13] , Rachael M. Roettenbacher[14] , Gail Schaefer[9] , Judit Sturmann[9], Laszlo Sturmann[9],
Samuel J. Swihart[15] , and Ming Zhao[16]

[1] Astronomy Department, University of Michigan, Ann Arbor, MI 48109, USA
[2] Center of Excellence in Information Systems, Tennessee State University, Nashville, TN 37209, USA
[3] Dept. of Astrophysical and Planetary Sciences, Univ. of Colorado, Boulder, CO 80309, USA
[4] Stellar Astrophysics Centre, Department of Physics and Astronomy, Aarhus University, Ny Munkegade 120, DK-8000 Aarhus C, Denmark
[5] Research School of Astronomy & Astrophysics, Australian National University, Canberra ACT 2611, Australia
[6] Physics Department, University of Michigan, Ann Arbor, MI 48109, USA
[7] Lunar and Planetary Laboratory, University of Arizona, Tucson, AZ 85721 USA
[8] Department of Physics and Astronomy, Georgia State University, Atlanta, GA, USA
[9] The CHARA Array of Georgia State University, Mount Wilson Observatory, Mount Wilson, CA 91203, USA
[10] Institute for Astronomy, University of Hawai'i, 2680 Woodlawn Drive, Honolulu, HI 96822, USA
[11] Sydney Institute for Astronomy (SIfA), School of Physics, University of Sydney, NSW 2006, Australia
[12] SETI Institute, 189 Bernardo Avenue, Mountain View, CA 94043, USA
[13] University of Exeter, School of Physics, Astrophysics Group, Stocker Road, Exeter EX4 4QL, UK
[14] Department of Astronomy, Stockholm University, SE-106 91 Stockholm, Sweden
[15] Department of Physics and Astronomy, Michigan State University, East Lansing, MI 48824, USA
[16] Department of Astronomy & Astrophysics, The Pennsylvania State University, 525 Davey Lab, University Park, PA 16802, USA

Abstract

Combining visual and spectroscopic orbits of binary stars leads to a determination of the full 3D orbit, individual masses, and distance to the system. We present a full analysis of the evolved binary system δ Delphini using astrometric data from the MIRC and PAVO instruments on the CHARA long-baseline interferometer, 97 new spectra from the Fairborn Observatory, and 87 unpublished spectra from the Lick Observatory. We determine the full set of orbital elements for δ Del, along with masses of $1.78 \pm 0.07\,M_\odot$ and $1.62 \pm 0.07\,M_\odot$ for each component, and a distance of 63.61 ± 0.89 pc. These results are important in two contexts: for testing stellar evolution models and for defining the detection capabilities for future planet searches. We find that the evolutionary state of this system is puzzling, as our measured flux ratios, radii, and masses imply a $\sim$200 Myr age difference between the components, using standard stellar evolution models. Possible explanations for this age discrepancy include mass transfer scenarios with a now-ejected tertiary companion. For individual measurements taken over a span of two years, we achieve $<10\,\mu$as precision on the differential position with 10 minute observations. The high precision of our astrometric orbit suggests that exoplanet detection capabilities are within reach of MIRC at CHARA. We compute exoplanet detection limits around δ Del and conclude that, if this precision is extended to wider systems, we should be able to detect most exoplanets $>2\,M_J$ on orbits >0.75 au around individual components of hot binary stars via differential astrometry.

Key words: astrometry – binaries: close – binaries: spectroscopic – binaries: visual – planets and satellites: detection

1. Introduction

Binary systems provide a unique opportunity to study the physical properties of stars. Combining spectroscopic and astrometric studies of binary stars allows one to determine the full 3D orbit of the system and obtain fundamental properties such as masses and distance. Systems for which both double-lined spectroscopic and visual orbits can be obtained are therefore valuable systems for the testing of stellar evolution models. Long-baseline interferometry provides the capability to resolve sub-arcsecond binary systems in order to obtain visual orbits of systems that would otherwise only be resolved through spectroscopic studies. Bonneau et al. (2014) give a thorough overview on how interferometric studies are combined with spectroscopy to determine the physical properties of both components in a binary system. In this paper, we use the Michigan Infra-Red Combiner (MIRC) on the Center for High Angular Resolution Astronomy (CHARA) Array long-baseline interferometer to obtain a precise visual orbit of the close

binary system δ Delphini (HR 7928, HD 197461). With this visual orbit, we achieve $<10\,\mu$as precision, maintained over two years, on many of the individual measurements of differential position.

Because of the short-period variations in its light curve, δ Del was first classified as a δ Scuti variable by Eggen (1956). Struve et al. (1957) confirmed this variable star classification through a spectroscopic study of δ Del. Neither of these studies detected the binarity of the system. As part of the Reports of Observatories, 1965–1966, published in The Astronomical Journal, Whitford reported in the Lick Observatory yearly summary that G. Preston had discovered δ Del to be a double-lined spectroscopic binary with a preliminary period of 40 days. The high eccentricity of the system produced double lines that are only visible for about three of the 40 days, which is the reason why previous observers had not discovered the binarity of the system. From an undergraduate thesis by Duncan in 1973, Duncan & Preston (1979) reported the results

of the first comprehensive study of δ Del as a binary system. Using Lick Observatory spectra, they obtained radial velocities (RVs) from which they determined a binary orbit with a period of 40.580 days and a high eccentricity of 0.7. They also found that both the primary (more massive) and secondary components show δ Scuti pulsations with dominant periods of 0.158 and 0.134 days, respectively. They concluded that the components were nearly equal in luminosity and temperature, but determined a mass ratio of ∼1.2. This made it impossible for Duncan and Preston to find locations in the Hertzsprung–Russell (HR) diagram that satisfied the constraints of mass ratio, luminosity, and the stars being the same age. In this paper, we combine our astrometric data from CHARA, RVs from 97 new spectra obtained at Fairborn Observatory, and the unpublished RVs from the 87 Lick Observatory spectra measured by Duncan & Preston (1979) to obtain a 3D orbit of δ Del. We also reassess the age and other properties of the system using stellar evolution models.

Along with our orbital study of δ Del, we use the <10 μas precision demonstrated on this system to explore the feasibility of detecting exoplanets around stars in a close binary system using MIRC at CHARA. A Jupiter-mass planet at a separation of 1 au imparts about a 10 μas wobble on a solar-mass host star at the distance of δ Del. Thus, with the precision of MIRC, we should be able to detect this wobble on a single component of a close binary system. Astrometric orbits of planets are desirable because they unveil important orbital parameters, such as the inclination of the orbit and true mass. Unlike RV or transit methods, astrometric detection is favorable for planets that have wider orbits. On the other hand, astrometry is sensitive to planets on somewhat tighter orbits than direct imaging surveys. Although this regime is comparable to that explored through microlensing techniques, astrometry has the advantage of repeat observations. Moreover, planet detection via differential astrometry with the use of long-baseline interferometry favors A- and B-type binary stars. This is a regime that is very difficult to explore with RV surveys because hot stars typically have weak and broad spectral lines. Transit surveys are also biased against hot stars because stellar pulsations and variability mask transit signals. Historically, the exoplanet field has been riddled with false claims of detection via astrometry (see Muterspaugh et al. (2010) for a brief overview). However, as instrumental precision continues to improve, astrometric detection of exoplanets is finally becoming feasible. By the end of its nominal five-year mission, *Gaia* is expected to reveal many new astrometric detections of giant exoplanets around mostly lower-mass stars (Casertano et al. 2008; Perryman et al. 2014; Sahlmann et al. 2014; Sozzetti et al. 2014). From the ground, long-baseline interferometry is a promising method for detecting exoplanets around intermediate mass stars in close binary systems. The Palomar High-precision Astrometric Search for Exoplanet Systems (PHASES) recently used long-baseline interferometry that led to the announcement of six substellar candidates to the individual components of binaries (Muterspaugh et al. 2010). In this paper, we show that the MIRC instrument at CHARA has achieved the precision needed for exoplanet detection around single stars in close (sub-arcsecond) binary systems.

This paper is organized as follows. Section 2 describes our observations and the subsequent data reduction. Section 3 then outlines our orbit fitting techniques, and Section 4 presents the best-fit orbital and physical parameters for the δ Del binary

Table 1
Log of MIRC Interferometric Observations

UT date	Baseline	No. of 10 s Averages	Calibrators[a]
2011 Jul 15	S2E1W1W2E2	168	a
2011 Jul 17	S1S2E1W1W2	80	b
2012 Jun 10	W1W2E2	48	c
2012 Jun 12	S1S2W1W2E2	160	d
2012 Jun 15	S1S2E1W1W2E2	120	e
2012 Jun 16	S1S2W1W2	48	f
2012 Jun 20	S1S2W1W2E2	80	g
2012 Sep 19	S1S2E1W1W2E2	120	h
2012 Sep 20	S1S2W1W2E2	80	i
2013 Jul 13	S2W1W2	24	a
2013 Jul 14	S1S2E1W1W2E2	120	e

Note.
[a] Refer to Table 2 for details of the calibrators used.

system. In Section 5, we use stellar evolution considerations to interpret the unusual positions of the δ Del components in the H–R diagram. The paper concludes, in Section 6, with a discussion of the corresponding limits on future exoplanet detections.

2. Observations and Data Reduction

2.1. Interferometry

Interferometric data for δ Del were collected in *H*-band on eleven nights from 2011 July 15 to 2013 July 14 with MIRC at the CHARA Array. The CHARA Array is an optical/near-IR interferometer with the longest baselines of any interferometer of its type in the world (ten Brummelaar et al. 2005). MIRC combines all six telescopes available at CHARA with baselines up to 330 m. The instrument is described in detail by Monnier et al. (2006). Additionally, *R*-band data were recently obtained with the Precision Astronomical Visible Observations (PAVO) instrument in 2017 June 14–17. PAVO is a visible light beam combiner on the CHARA array that is predominantly used for two-telescope observations. The PAVO instrument and data reduction techniques are described further in Ireland et al. (2008). Observational details and calibrators used for MIRC are displayed in Tables 1 and 2, while those for PAVO are given in Tables 3 and 4. The angular diameters for the calibrators in Table 4 were obtained from the $V - K$ surface brightness relation of Kervella et al. (2004).

We used the MIRC combiner to measure visibilities and closure phases of δ Del. Amplitude calibration was performed through use of a beamsplitter following spatial filtering. Observations of reference calibrators are made throughout the night to correct for time-variable factors such as atmospheric coherence time, vibrations, differential dispersion, and birefringence in the beam train. Using the standard data pipeline as described in earlier MIRC papers (e.g., Monnier et al. 2012), we produce a calibrated OI-FITS file (Pauls et al. 2005) for each night (available upon request). For each night, we fit a binary model with the following free parameters: Uniform Disk (UD) diameter of component 1, UD diameter of component 2, *H*-band flux ratio of component 1 over component 2, angular separation, position angle (PA) of vector pointing from component 1–2 (east of north). To estimate errors, we derive a χ^2 surface for a grid in relative right ascension (R.A.) and declination (decl.) and find the $1-\sigma$ confidence contour

Table 2
Calibrators Used for MIRC Interferometric Observations

HD	Sp. type	H (mag)	θ_{UD} (mas)	Source for UD	ID
205776	K2III	4.138	0.79 ± 0.055	Chelli et al. (2016)	a
886	B2IV	3.43	0.41 ± 0.03	Barnes et al. (1978)	b
135742	B8Vn	2.8	0.645 ± 0.045	Chelli et al. (2016)	c
165777	A5V	3.426	0.68 ± 0.06	Chelli et al. (2016)	d
187691	F8V	3.863	0.7 ± 0.04	Chelli et al. (2016)	e
185395	F3+V	3.716	0.726 ± 0.014	White et al. (2013)	f
161868	A1VnkA0mA0	3.64	0.571 ± 0.04	Chelli et al. (2016)	g
6920	F8V	4.493	0.539 ± 0.037	Chelli et al. (2016)	h
195810	B6III	4.55	0.35 ± 0.05	Barnes et al. (1978)	i

Table 3
Log of PAVO Interferometric Observations

UT date	Baseline[a]	No. of scans	Calibrators[b]
2017 Jun 14	E2W1	3	cd
2017 Jun 15	E1W2	3	cd
2017 Jun 17	E2W2	5	cd
2017 Jun 18	S1W2	3	abcd
2017 Jun 19	W1W2	3	ac

Notes.
[a] The baselines used have the following lengths: W1W2, 107.92 m; E2W2, 156.27 m; S1W2, 210.97 m; E1W2, 221.82 m; E2W1, 251.33 m.
[b] Refer to Table 4 for details of the calibrators used.

Table 4
Calibrators Used for PAVO Interferometric Observations

HD	Sp. type	V	$V-K$	A_V	θ_{V-K}	ID
195943	A3IVs	5.380	0.138	0.089	0.299	a
196775	B3V	5.960	−0.473	0.261	0.153	b
196821	A0III	6.075	0.034	0.000	0.204	c
201616	A2Va	6.057	0.117	0.000	0.218	d

(approximated by an "error ellipse" with a major axis, minor axis, and PA of major axis)—for this, we made a simple assumption that the errors in all wavelength channels are correlated. Because we lack a full covariance matrix, we consider this error analysis a first estimate and will adjust the scale of the errors' ellipses by a scalar factor later in the analysis as we fit the binary orbit. The results from this analysis can be found in Table 5. Note that, because of different (u,v) coverages and seeing conditions, the errors vary strongly between the different nights. Visibilities and closure phases from MIRC for UT 2012 June 15, visibilities from PAVO for UT 2017 June 14, and the best-fit models are shown in Figure 1.

The stellar angular diameters and flux ratio between components were poorly constrained on individual nights. To improve our estimate, we used the final orbit (derived in Section 4.2) to allow a global fit for the diameters and flux ratio, under the assumption they do not vary (although this is not strictly true because of the δ Scuti pulsations). From the orbit, we fixed the orbital geometry and then fitted the angular diameters and flux ratio with the full data set, using bootstrap sampling to estimate our errors. Table 6 contains the results of this work: UD1 (brighter star) 0.49 ± 0.03 mas, UD2 (fainter star) 0.49 ± 0.03 mas, flux ratio 1.04 ± 0.03. These errors include uncertainties on the wavelength scale (±0.25%) and on the calibrator diameters.

To improve our diameter estimates, we also collected single-baseline observations of δ Del with the visible-light PAVO combiner. The individual nights did not have sufficient (u, v) coverage to simultaneously constrain relative positions as well as the stellar properties. Following a procedure similar to MIRC, we used the precise orbit predictions from our model to fix the orbital geometry for the five nights of PAVO observations. We then did a global least-squares fit (and bootstrap) with the following free parameters: UD diameter of component 1, UD diameter of component 2, and R-band flux ratio of component 1 over component 2. The best-fit reduced χ^2 was 2.5, higher than normal, which may be due to uncertainty in the wavelength scale of PAVO (±0.6%) being unaccounted for. Table 6 also contains the PAVO results: UD1 (brighter star) 0.460 ± 0.014 mas, UD2 (fainter star) 0.510 ± 0.014 mas, Flux ratio 1.10 ± 0.05. These errors include uncertainties on the wavelength scale (±0.6%) and on the calibrator diameters (5%).

Lastly, we needed to determine our final estimate of the effective temperatures for the two components of δ Del. To do this, we used Kurucz/Castelli models[17] (Castelli & Kurucz 2004) to fit for the limb-darkening corrected R- and H-band diameters determined from interferometry, the interferometrically determined component flux ratios, and literature photometry $R = 4.17 \pm 0.05$ (Morel & Magnenat 1978), $H = 3.70 \pm 0.24$ (Cutri et al. 2003). We found an acceptable fit with the following stellar parameters: Component 1: LD diameter 0.500 ± 0.014 mas, Temperature 7440 K ± 210 K; Component 2: LD diameter 0.507 ± 0.014 mas, Temperature 7110 K ± 180 K. These parameters, along with physical radii, luminosity, and component R/H magnitudes, can be found in Table 6. We will use these properties to create an HR diagram in Section 5.

2.2. Spectroscopy

We acquired 97 useful spectroscopic observations of δ Del between 2012 June and 2016 June, using the Tennessee State University 2 m Automatic Spectroscopic Telescope (AST) and a fiber-fed echelle spectrograph (Eaton & Williamson 2007) that is located at Fairborn Observatory in southeast Arizona. The detector was a Fairchild 486 CCD that has a 4096 × 4096 array of 15 micron pixels. The echelle spectrograms have 48 orders that cover a wavelength range from 3800 to 8260 Å. Our observations were made with a fiber that produces a resolution of 0.24 Å, and the spectrograms have typical signal-

---

[17] Specifically, we used the tables found at: https://www.oact.inaf.it/castelli/castelli/grids/gridp00k2odfnew/fp00k2tab.html and https://www.oact.inaf.it/castelli/castelli/grids/gridm05k2odfnew/fm05k2tab.html.

Table 5
δ Del Astrometry Data

UT Date	MJD	sep (mas)	P.A. (°)	Error Major Axis (mas)	Error Minor Axis (mas)	Error Ellipse P.A. (°)
2011 Jul 15	55757.331	7.166	337.31	0.004	0.002	302
2011 Jul 17	55759.323	6.448	345.80	0.003	0.001	319
2012 Jun 10	56088.492	4.274	15.80	0.049	0.009	341
2012 Jun 12	56090.483	2.961	46.79	0.008	0.002	64
2012 Jun 15	56093.450	2.120	170.36	0.004	0.003	287
2012 Jun 16	56094.503	2.750	206.10	0.033	0.005	40
2012 Jun 20	56098.446	5.363	256.94	0.012	0.011	56
2012 Sep 19	56189.215	8.449	295.20	0.015	0.009	276
2012 Sep 20	56190.219	8.570	297.96	0.005	0.004	37
2013 Jul 13	56486.512	7.662	331.29	0.07	0.016	38
2013 Jul 14	56487.351	7.430	334.10	0.005	0.003	337

to-noise ratios of 70–130. Fekel et al. (2013) have provided additional information about the facility.

Fekel et al. (2009) gave a general explanation of the velocity measurement of the AST echelle spectrograms. For δ Del, we used our solar-type star line list that contains 168 lines in the wavelength range 4920–7100 Å. At our resolution, the lines of the two components at maximum velocity separation are almost completely resolved. At most other phases, the features are very significantly blended—as can be seen in Figure 2. We used rotational broadening functions (Fekel & Griffin 2011; Sandberg Lacy & Fekel 2011) to simultaneously fit the line pairs. Because of pulsation, the shapes of the lines vary to some extent from spectrum to spectrum. Therefore, although we used the average width and depth values from our most widely separated line pairs as starting values for our velocity determinations, those two parameters were not fixed in our fits. To test for systematics affecting our RV determinations for this blended system, we divided our line list into blue (4920–5501 Å) and red (5506–7200 Å) halves and remeasured velocities for six spectra near maximum velocity separation and 10 spectra near the lower velocity separation. After comparing RVs determined from the red half, the blue half, and the full wavelength range, we see no striking systematics in our results.

Our unpublished velocity measurements of several IAU RV standards from spectra obtained with our 2 m AST have an average velocity difference of $-0.6 \, \mathrm{km \, s^{-1}}$ when compared to the results of Scarfe (2010). Thus, we have added 0.6 km s^{-1} to each of our measured velocities. The 97 Fairborn RVs used for orbit fitting are listed in Table 7. In addition to these velocities, we measured two single-lined spectra from the 2 m AST to determine velocities very close to the phase of the center-of-mass velocity. At MJD 56197.2428, we obtain a single-lined RV of 10.4 km s^{-1}, and we obtain a velocity of 8.8 km s^{-1} at MJD 57090.5220. We did not include these two points in the fitting routine because the precision of these measurements is lacking due to δ Scuti pulsations and different rotational velocities of the components. However, the positions of these single-lined velocities appear to support the system velocity and mass ratio obtained in our best-fit orbit described in Section 4.2.

From our fits to the lines in our Fairborn Observatory spectra that are at phases near maximum velocity separation, we have determined $v \sin i$ values of $17 \pm 1 \, \mathrm{km \, s^{-1}}$ for the more massive primary star and $12 \pm 1 \, \mathrm{km \, s^{-1}}$ for the less massive secondary. For the same subset of spectra that we used to determine the $v \sin i$ values of the components, we measured the average line equivalent widths of the two stars. That ratio, which corresponds to the luminosity ratio of the components for stars of similar temperature,

was highly variable—probably because of the rather significant δ Scuti pulsations, which also affect the line profiles. With the ratio of the more massive primary to the less massive secondary ranging from 1.2 to 0.9, the average ratio is 1.03 ± 0.02 for a central wavelength of 6000 Å. Thus, we henceforth assume that the more massive star is also the brighter component.

At the Lick Observatory, 87 spectra of δ Del were obtained with the 120 inch telescope at a dispersion of 5.3 Å mm^{-1}. Ten lines in the wavelength range 3900–4300 Å were used to determine RVs for both components. Velocity measurements were made with a Grant measuring engine and reduced with a standard computer program. These RVs, which are presented in Table 8 and have not been published until now, only cover phases very close to maximum velocity separation. We use the RVs of both components from the 87 observations acquired at Lick Observatory, as well as the 97 new observations obtained at Fairborn Observatory, when carrying out our orbital fitting routines.

3. Orbit Fitting Routine

3.1. Astrometry Model

The Campbell elements (ω, Ω, e, i, a, T, P) describe the motion of one star of a binary relative to the other. Those symbols have their usual meanings, where ω is the longitude of the periastron, Ω is the PA of the ascending node, e is the eccentricity, i is the orbital inclination, a is angular separation, T is the time of periastron passage, and P is orbital period. Good overviews for the use of least-squares fitting to determine the best fit orbital elements are given by Wright & Howard (2009) and Lucy (2014). The errors in our positions for δ Del are ellipses, and thus, to determine the best-fit orbital elements with a least-squares routine, we must project the residuals into the major and minor ellipse axes when defining χ^2. We define χ^2 in the major and minor axes as

$$\chi^2_{\mathrm{major}} = \frac{[(x_{\mathrm{data}} - x_{\mathrm{model}})\sin\sigma_{\mathrm{pa}} + (y_{\mathrm{data}} - y_{\mathrm{model}})\cos\sigma_{\mathrm{pa}}]^2}{\sigma^2_{\mathrm{major}}}$$

$$\chi^2_{\mathrm{minor}} = \frac{[-(x_{\mathrm{data}} - x_{\mathrm{model}})\cos\sigma_{\mathrm{pa}} + (y_{\mathrm{data}} - y_{\mathrm{model}})\sin\sigma_{\mathrm{pa}}]^2}{\sigma^2_{\mathrm{minor}}},$$

(1)

where σ_{pa}, σ_{major}, and σ_{minor} are the error ellipse PA, error in major axis, and error in minor axis, respectively. The final positions predicted by our model are given by x_{model} and y_{model}, while x_{data} and y_{data} are the positions measured by MIRC. The total χ^2 for the astrometry data is then just the sum of χ^2_{major}
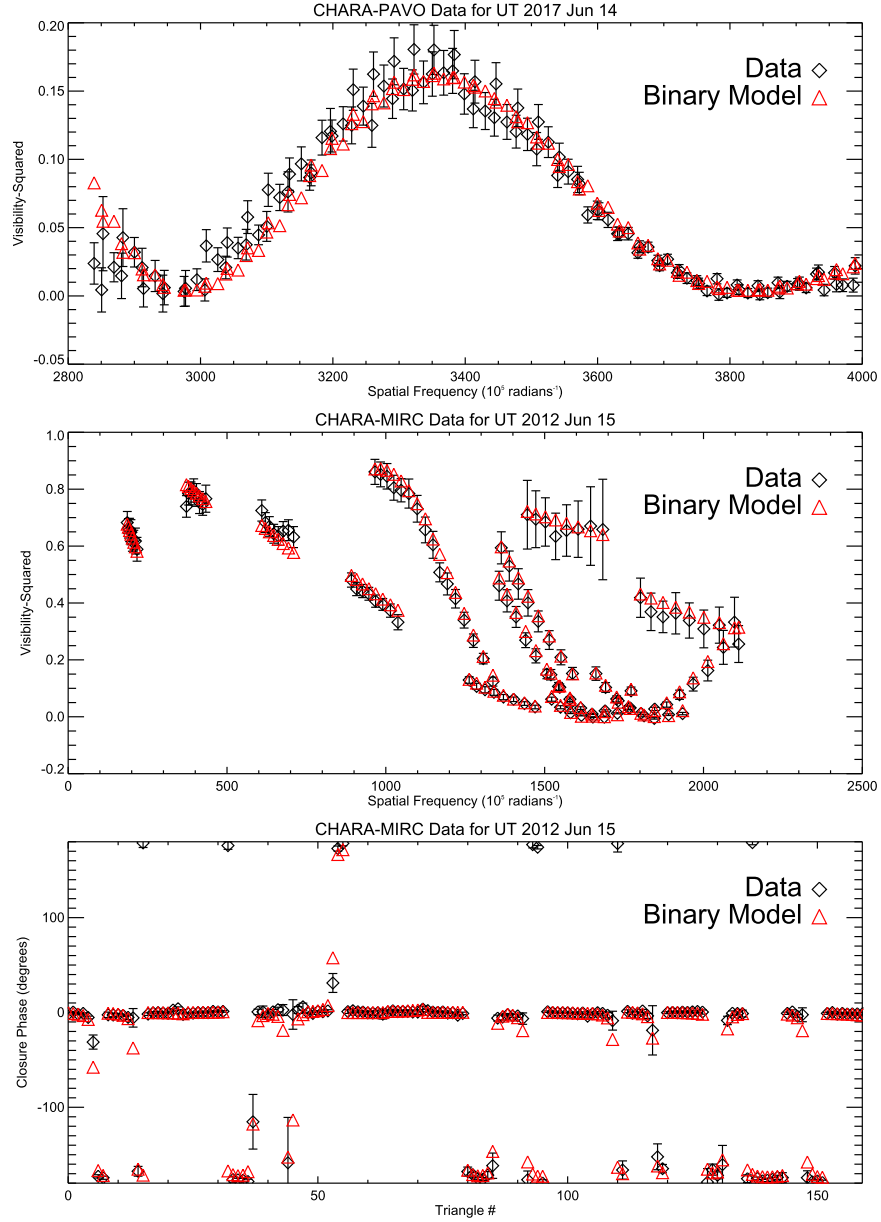
Figure 1. Squared visibilities are plotted along with the best-fit binary model on a single night for the PAVO and MIRC interferometric data. For the MIRC data, we also plot closure phases for a single night. The "Triangle #" is a combination of time, geometry (which closing triangle is being used), and wavelength.

Table 6
δ Del Stellar Properties

	Component 1	$\cdots$	Component 2
$f_1/f_{2\ H\text{-band}}$	$\cdots$	1.04 ± 0.03	$\cdots$
$f_1/f_{2\ R\text{-band}}$	$\cdots$	1.10 ± 0.05	$\cdots$
H (mag)	4.43 ± 0.24		4.47 ± 0.24
R (mag)	4.87 ± 0.03		4.98 ± 0.03
$\theta_{\text{UD }H\text{-band}}$ (mas)	0.49 ± 0.03		0.49 ± 0.03
$\theta_{\text{UD }R\text{-band}}$ (mas)	0.460 ± 0.014		0.510 ± 0.014
θ_{LDD} (mas)	0.500 ± 0.014		0.507 ± 0.014
Radii ($R_\odot$)	3.43 ± 0.11		3.48 ± 0.11
Temperature (K)	7440 ± 210		7110 ± 180
Luminosity ($L_\odot$)	32.4 ± 4.2		28.8 ± 3.4

and χ^2_{minor}. The reduced χ^2 for our best fit suggests that astrometry error values are overestimated. We reduce the error values by a factor of $\sim$3.5 to bring the reduced χ^2 to 1. This

ensures that one data set is not unevenly weighting the fitting when combining astrometry and RV data.

3.2. RVs Model

The orbital elements for the double-lined spectroscopic binary are ω, e, K_1, K_2, γ, T, and P. The elements ω, e, T, and P are the same as presented in the astrometry model, K_1 and K_2 are the velocity semi-amplitudes of each component, and γ is the systemic velocity. These elements are used to compute a model value for velocity at each time of observation. Once again, the total χ^2 for RV data is just the sum of the individual components, χ^2_{primary} and $\chi^2_{\text{secondary}}$. The Fairborn RVs cover a much more extensive portion of the full orbit, and each velocity is the average of a much greater number of lines, so we assign these velocities twice the weight of those obtained at Lick Observatory. Because the reduced χ^2 for the RV best fit is >1, we increase the RV error values by a factor of $\sim$1.3 to bring the
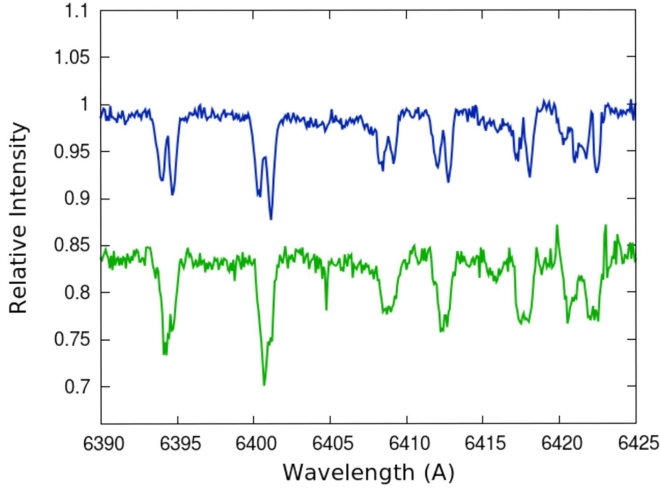
Figure 2. Plotted are partial spectra from the Fairborn Observatory for δ Del at maximum velocity separation and at lower velocity separation. At maximum velocity separation (top spectrum) the peaks from the two components are almost completely resolved. This gives us good constraints on the line width and depth, enabling reliable fits also at the epochs with smaller velocity separation, when the lines are blended (bottom spectrum).

reduced χ^2 to 1, to facilitate fitting the combined RV and astrometry data.

3.3. Fitting Methods

We use a Markov chain Monte Carlo (MCMC) fitting routine to determine the best-fit parameters for our binary model. An MCMC fit can efficiently sample a large region of parameter space to ensure that a global minimum has been reached, unlike the least-squares method, which can become stuck at local minima solutions. Parameter distributions from the MCMC sampling also provide more accurate error values than those obtained via least-squares fitting. We carry out an MCMC fit using the Python package *emcee* developed by Foreman-Mackey et al. (2013).

Assuming independent Gaussian errors for our data, the log-likelihood function is given simply as

$$\ln(\mathcal{L}) = -\frac{1}{2}\chi^2, \qquad (2)$$

where χ^2 is formulated as explained in the previous subsections. As a starting point for our MCMC walkers, we use the Python package *lmfit* for non-linear least squares fitting (Newville et al. 2014). To sample a large amount of parameter space, we randomly perturb each parameter around its best-fit value, using the least-squares as a starting point for each walker. For each fit, we run 2^*N_{params} walkers until convergence is reached. The Gelman-Rubin diagnostic (Gelman & Rubin 1992) is used to test whether or not a chain has converged. This diagnostic checks the variance of a parameter in one chain against the variance between chains, and is given by

$$R = \sqrt{\frac{\text{Var}(\Theta)}{W}}, \qquad (3)$$

where Θ is some parameter and W is the variance within a single chain. As a chain converges, this ratio approaches unity. In the results presented, all of our chains have been run until

Table 7
δ Del Radial Velocities from Fairborn Observatory

MJD	$v_1 \, [\pm 1.3]$ (km s^{-1})	$v_2 \, [\pm 0.7]$ (km s^{-1})	v_1 (δ Scuti subtracted)
56100.194	20.2	−0.6	19.7
56101.23	18.9	1.2	18.0
56101.305	18.2	0.7	19.0
56106.306	16.6	3.3	15.8
56107.345	16.0	4.0	15.1
56126.284	−0.3	18.5	1.6
56168.311	−2.6	20.6	−1.1
56169.306	1.0	24.0	−1.3
56172.306	−5.9	28.0	−7.4
56173.306	−4.9	25.7	−2.4
56261.174	19.3	−2.0	17.3
56262.168	18.2	−1.4	18.4
56266.142	16.7	1.5	18.7
56267.141	17.7	3.3	15.4
56415.456	−4.9	26.9	−6.9
56547.301	19.0	−0.3	18.3
56547.343	20.4	−1.5	18.3
56547.366	19.1	−0.2	18.7
56549.149	14.9	0.8	17.0
56574.09	0.9	22.8	2.3
56575.101	1.3	21.7	−0.5
56576.106	−6.5	26.2	−4.0
56577.089	−4.7	27.4	−5.1
56577.104	−3.3	27.1	−5.0
56577.204	−7.7	26.3	−5.2
56578.088	−8.1	28.6	−9.4
56578.204	−7.1	28.6	−8.9
56579.087	−10.2	27.6	−7.8
56583.084	21.5	−2.0	19.2
56584.094	16.6	−1.7	19.0
56585.082	18.0	−1.2	17.9
56586.112	17.6	−1.6	18.9
56623.097	20.0	0.2	19.6
56624.17	22.0	−1.7	19.8
56736.481	−6.2	18.1	−4.6
56737.501	−4.4	19.6	−6.0
56740.469	−8.1	26.5	−8.8
56741.46	−5.4	25.8	−7.1
56742.492	2.0	18.3	2.8
56744.471	20.2	1.2	21.4
56745.448	17.4	−1.1	19.7
56747.455	19.2	0.0	20.8
56776.348	−1.4	18.6	0.3
56777.369	0.9	22.4	−0.5
56778.457	1.3	24.2	−0.7
56779.367	−2.0	25.1	−3.7
56780.328	−1.5	28.4	−3.8
56781.337	−11.9	27.5	−9.5
56782.336	−4.1	25.9	−5.0
56785.329	20.1	−0.9	18.1
56786.309	22.4	−2.0	21.2
56787.337	21.6	−1.8	22.2
56788.318	22.0	−1.6	19.7
56789.3	19.7	−1.6	19.6
56822.212	−7.3	29.1	−8.7
56822.255	−8.7	28.5	−6.5
56823.212	−6.6	24.1	−4.2
56826.255	20.5	−2.3	18.4
56826.288	20.7	−1.7	19.3
56827.255	18.5	−1.9	19.5
56827.288	18.5	−1.6	20.9
56828.294	21.8	−1.2	19.7
56829.326	15.8	−1.9	18.2

Table 7
(Continued)

MJD	v_1 [$\pm$1.3] (km s^{-1})	v_2 [$\pm$0.7] (km s^{-1})	v_1 (δ Scuti subtracted)
56830.323	21.4	−0.6	19.8
56831.287	20.0	−1.4	17.7
56899.285	−0.6	22.9	0.1
56944.086	−9.6	30.2	−7.3
56945.133	0.0	24.4	−1.6
56954.19	19.5	0.3	17.7
57103.516	−4.9	23.1	−4.6
57115.506	18.5	−0.8	18.8
57143.489	−2.2	21.9	−2.7
57184.291	−5.2	23.1	−2.9
57185.354	−3.7	24.9	−4.1
57186.354	−9.5	27.8	−7.5
57187.355	−6.4	28.6	−8.7
57188.355	−7.1	25.8	−5.5
57192.375	22.7	−0.8	20.4
57347.068	−2.8	25.7	−0.8
57348.075	−2.9	25.6	−5.2
57349.082	−9.6	27.0	−7.2
57350.069	−9.3	28.4	−9.2
57351.07	0.2	24.8	−1.4
57356.067	20.4	−2.9	18.1
57511.352	−9.5	26.2	−7.6
57512.316	−10.2	29.0	−7.8
57513.334	0.1	24.6	−2.2
57516.307	20.6	−0.1	18.3
57517.306	18.9	−0.7	20.6
57518.304	20.2	−1.8	20.6
57519.34	18.2	−1.4	19.5
57520.329	19.1	−0.6	20.6
57551.217	−8.3	26.5	−6.8
57552.219	−5.1	26.8	−7.4
57553.221	−10.5	27.5	−8.3
57557.219	23.3	−0.6	21.2
57558.243	15.8	−2.2	18.2

Table 8
δ Del RVs Obtained from the Lick Observatory

MJD	v_1 [$\pm$2.6] (km s^{-1})	v_2 [$\pm$1.3] (km s^{-1})	v_1 (δ Scuti subtracted)	v_2 (δ Scuti subtracted)
38306.242	−9.5	29.9	−9.1	28.5
39238.541	−7.6	25.6	−5.5	26.6
39239.409	−5.8	28.3	−9.1	27.0
39239.442	−6.8	26.4	−8.2	26.9
39239.452	−8.8	27.1	−9.1	28.0
39239.467	−10.8	27.4	−9.6	28.4
39239.474	−11.1	27.7	−9.3	28.5
39239.51	−7.7	29.4	−6.4	28.3
39239.516	−8.0	28.4	−7.3	27.1
39239.522	−7.1	28.4	−7.0	27.0
39279.447	−8.3	28.9	−7.2	28.6
39280.303	−5.2	28.4	−6.8	28.0
39280.317	−2.9	30.3	−5.7	30.7
39280.359	−2.3	30.2	−4.2	30.7
39280.362	−6.1	30.2	−7.7	30.5
39280.373	−9.0	28.9	−9.5	28.6
39280.382	−8.6	29.6	−8.0	28.8
39280.39	−8.2	29.7	−6.9	28.5
39280.398	−8.0	30.2	−6.1	28.8
39280.408	−8.4	32.5	−6.2	31.0
39280.415	−8.6	33.6	−6.4	32.3
39280.423	−9.8	32.1	−7.8	31.0
39280.43	−10.5	30.9	−9.0	30.2
39280.436	−10.8	29.9	−9.9	29.6
39280.442	−11.2	29.7	−10.9	29.7
39280.45	−9.9	29.0	−10.4	29.4
39280.456	−9.0	27.9	−10.1	28.6
39280.462	−8.3	27.8	−10.1	28.7
39281.356	−8.8	28.3	−6.6	27.6
39362.232	−9.8	28.8	−8.7	29.7
39362.247	−11.6	28.2	−9.5	28.5
39362.259	−10.4	29.0	−8.2	28.6
39362.27	−9.0	28.7	−7.2	27.7
39362.282	−0.7	29.5	0.1	28.1
39362.298	−4.3	28.4	−5.2	27.0
39362.312	−4.3	27.3	−6.6	26.5
39362.324	−4.5	25.9	−7.6	25.7
39362.335	−5.6	28.6	−8.9	29.0
39362.346	−5.4	27.1	−8.4	28.0
39362.359	−5.2	27.2	−7.2	28.2
39362.373	−7.0	25.6	−7.6	26.2
39362.386	−9.2	27.8	−8.4	27.7
39362.41	−12.5	27.7	−10.3	26.4
39362.422	−11.8	28.3	−9.8	26.8
39362.435	−9.1	27.2	−7.9	25.9
39401.111	−5.9	25.4	−5.3	26.4
39401.132	−3.5	26.9	−1.4	27.6
39401.152	−6.2	28.5	−4.3	28.1
39401.256	−7.2	27.0	−7.9	27.9
39401.269	−8.1	27.0	−7.4	27.5
39401.282	−6.4	26.9	−4.6	26.6
39401.34	−6.4	26.8	−7.4	26.1
39402.098	−10.9	29.5	−9.3	28.2
39402.165	−3.2	27.3	−6.4	28.2
39402.175	−5.3	27.9	−8.1	28.9
39402.222	−9.5	29.2	−7.7	28.1
39402.231	−9.7	29.6	−7.5	28.2
39402.239	−7.9	30.0	−5.7	28.5
39402.319	−3.3	27.8	−6.6	28.6
39402.333	−3.3	29.2	−6.0	29.4
39726.278	−2.1	24.2	−3.2	25.2
39726.284	−3.0	24.3	−3.5	25.2
39726.289	−7.1	25.3	−7.0	26.1

$R < 1.001$. Uniform priors are used for each parameter, with search range restrictions given in Table 9.

The orbital elements can be determined from separate fits to astrometry and RV data, or from combining the data sets to fit all 10 orbital parameters at once. In the next section, we present fitting results for all three cases (astrometry alone, RV alone, and combined fit). The results of our fitting routines for δ Del are also presented in the next section.

4. Orbital Fitting Results

4.1. Astrometry Alone

Using our described fitting routine, we first determine the best-fit orbital elements from astrometry data alone. The best-fit orbit and our measured positions are shown in Figure 3. Also plotted is the line of nodes along which the binary orbit is inclined. Data points near the nodes are crucial for constraining the angular semimajor axis, while points away from the nodes help constrain the inclination. The best-fit parameters and their errors from MCMC fitting are displayed in Table 10. Figure 4 shows parameter posterior distributions. Correlations between T and P, ω and Ω, and a and i are expected from a visual orbit. Our quoted error bar on each parameter is the standard deviation of the posterior distribution from the MCMC routine.

Table 8
(Continued)

MJD	v_1 [±2.6] (km s^{-1})	v_2 [±1.3] (km s^{-1})	v_1 (δ Scuti subtracted)	v_2 (δ Scuti subtracted)
39726.297	−7.4	27.0	−6.5	27.4
39726.305	−9.3	27.5	−7.7	27.5
39726.31	−9.9	27.8	−8.0	27.5
39726.316	−10.9	27.6	−8.8	27.0
39726.322	−9.8	28.0	−7.6	27.0
39726.323	−9.9	28.9	−7.7	27.9
39726.333	−9.5	28.2	−7.5	26.8
39726.338	−8.6	29.3	−6.9	27.8
39726.344	−6.0	28.9	−4.7	27.4
39726.351	−5.2	29.7	−4.5	28.3
39726.365	−3.4	29.8	−4.3	29.0
39726.384	−5.5	26.1	−8.2	26.4
39726.396	−3.3	26.3	−6.6	27.1
39726.406	−3.6	25.3	−6.9	26.3
39726.421	−2.0	26.2	−4.5	27.0
39726.438	−5.2	26.8	−6.0	26.8
39727.345	−7.4	29.4	−10.7	30.2
39727.426	−11.8	28.6	−9.6	27.9
39727.438	−9.3	28.2	−7.8	28.3
39727.451	−6.1	28.5	−5.7	29.2
39728.252	−9.1	24.5	−10.6	25.4
40781.310	−10.8	30.5	−12.9	29.3
40782.270	−10.2	29.7	−10.3	28.7

Table 9
MCMC Parameter Search Range

Parameter	Min Value ($>$)	Max Value ($<$)
P (days)	40	41
T (MJD)	56823	56825
e	0	1
ω (deg)	0	360
Ω (deg)	0	360
i (deg)	0	180
a (mas)	5.0	6.0
K_1 (km s^{-1})	0	30
K_2 (km s^{-1})	0	30
γ (km s^{-1})	0	30

Along with the MCMC error, there is a systematic error of $\pm0.25\%$ on the angular semimajor axis due to MIRC absolute wavelength calibration (Monnier et al. 2012).

4.2. RV Alone

Due to short period variations in their RV curves, both components of δ Del have been previously classified as δ Scuti variables with periods of 0.158 ± 0.006 days for the primary (more massive) component and 0.134 ± 0.015 days for the secondary (Duncan & Preston 1979). Though modeling these pulsations does not change the final orbital solution, we do detect δ Scuti variations in portions of our data. We detect significant period signals for the primary component in the Fairborn and Lick Observatory data, as well as for the secondary component in the Lick Observatory data. We describe our first-order corrections for these pulsations in the Appendix, and we list the resulting corrected RVs in Tables 7 and 8. Once the δ Scuti pulsations are subtracted out of the RV data, we determine the best-fit orbital elements to the RV data alone, using our MCMC routine. Figure 5 shows our best-fit
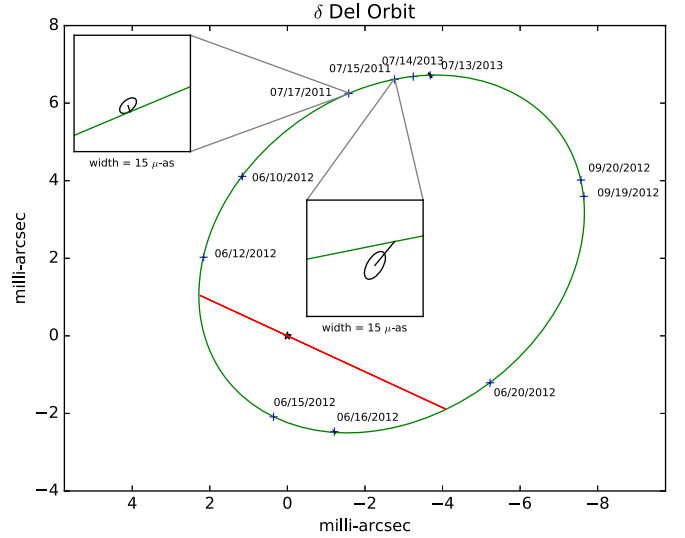
Figure 3. The position of the primary component relative to its companion at the origin. The green ellipse is the best-fit orbit for δ Del, determined by fitting to astrometry data. The error ellipses on each observation are too small to be seen at this scale, so the insets display representative errors. The red line is the line of nodes along which the orbit is inclined. Orbital motion is counterclockwise, with the portion of the orbit above the line of nodes inclined toward the observer and the portion below the line inclined away.

orbit with residual plots shown in Figures 6 and 7. These include the 97 double-line RV points from Fairborn Observatory, as well as the 87 data points from Lick Observatory. We also plot the two velocities measured from single-lined spectra near phase 0.6. These velocities are not included in the fit, due to the low precision of these points. However, the two velocities appear to support our best-fit values of system velocity and hence mass ratio. Figure 8 displays parameter posterior distributions. Table 10 shows the best-fit orbital elements from fitting to RV data alone, along with MCMC error values. Duncan & Preston (1979) reported values of 40.580 ± 0.003 and 0.7 ± 0.1 for the period and eccentricity in their preliminary orbit analysis. Our best value of 40.6051 ± 0.0002 days for the orbital period differs slightly from theirs, while our eccentricity of 0.632 ± 0.004 is within their quoted uncertainty.

4.3. Combined Fit with Physical Orbital Parameters

Because orbital elements ω, e, T, and P are constrained by both astrometry and RV data, it is advantageous to combine the data sets for a single fit. When combining data sets, we assign a weight to each set, in order to bring both reduced $\chi^2_{\rm ast}$ and $\chi^2_{\rm RV}$ to 1 when fitting separately. The total χ^2 to be minimized is

$$\chi^2_{\rm combined} = w_{\rm ast} * \chi^2_{\rm ast} + w_{\rm RV} * \chi^2_{\rm RV}, \qquad (4)$$

where $w_{\rm ast}$ and $w_{\rm RV}$ are the weights assigned to the astrometry and RV data sets. Table 10 shows the best-fit values for all ten orbital parameters determined from fitting to the combined set of data. Figure 9 shows the parameter distribution from our MCMC fitting routine. Note that there is a $\pm0.25\%$ wavelength calibration systematic error on the angular semimajor axis, as mentioned in Section 4.1. This systematic error affects the distance value determined from the orbit.

Combining astrometry and RV data leads to a measurement of physical orbital elements of parallax, linear semimajor axis,

Table 10
Best-fit Orbital Elements from Astrometry and RV Data

	Astrometry Alone	RV Alone	Astrometry+RV
P (day)	40.60510 ± 0.00015	40.60514 ± 0.00016	40.60505 ± 0.00014
T (MJD)	56823.604 ± 0.030	56823.6180 ± 0.032	56823.5019 ± 0.0028
e	0.6319 ± 0.0043	0.6334 ± 0.0046	0.64008 ± 0.00018
$\omega(°)$	67.17 ± 0.58	66.94 ± 0.61	65.07 ± 0.32
$\Omega(°)$	65.17 ± 0.58	$\cdots$	63.73 ± 0.33
$i(°)$	14.08 ± 0.19	$\cdots$	13.92 ± 0.18
a (mas)	5.4707 ± 0.0039[a]	$\cdots$	5.4676 ± 0.0037[a]
K_1 (km s^{-1})	$\cdots$	13.98 ± 0.14	13.88 ± 0.14
K_2 (km s^{-1})	$\cdots$	15.26 ± 0.07	15.27 ± 0.07
γ (km s^{-1})	$\cdots$	9.61 ± 0.07	9.48 ± 0.07

Note.
[a] ± 0.014 (systematic).

and masses of each component (see Torres et al. 2010 for relevant equations). These values and their errors are shown in Table 11. Our results agree with the original parallax measurement by *Hipparcos* of 16.03 ± 0.68 mas (Perryman et al. 1997). However, the revised *Hipparcos* reduction for δ Del reports a parallax of 14.61 ± 0.2 mas (van Leeuwen 2007), which is not consistent with our measurement. Our new parallax measurements decreases the *Hipparcos* distance of δ Del from 68.45 ± 0.94 pc to our new value of 63.61 ± 0.89 (± 0.16 systematic error) pc. Because *Hipparcos* did not identify this source as a binary, there could be systematic errors in the parallax determination, as photocenter motion due to binarity could effect the parallax fit. However, because the magnitudes are nearly equal in the *R*-band, one would not expect a large photocenter shift. We point out that a discrepancy from the revised *Hipparcos* reduction has been reported before, in the close binary system ψ Persei (Mourard et al. 2015).

Note that we present the results of fits carried out from velocities with the δ Scuti pulsations subtracted. However, we also carried out a combined fit using the measured RVs without the δ Scuti RV variations subtracted. None of the orbital elements or masses, nor the mass ratio, changed outside of the error bars quoted in the best-fit solution with the δ Scuti variations subtracted.

5. Stellar Evolution for δ Del

5.1. Rotational Velocities and Orbital Evolution

From our fits to the lines in our Fairborn Observatory spectra that are at phases near maximum velocity separation, we have determined $v \sin i$ values of 17 ± 1 km s^{-1} for the more massive primary star and 12 ± 1 km s^{-1} for the less massive secondary. If the rotational and orbital axes are parallel, as is usually assumed, then we can use our orbital inclination value of $13°9$ to determine the equatorial rotational velocities of the components. With that inclination, the projected velocities increase to 71 and 50 km s^{-1}, respectively.

Over time, the orbits of close binaries tend toward circularization, and rotational synchronization with the orbital period occurs for the components (e.g., Zahn 1977; Tassoul 1987; Tassoul & Tassoul 1992; Matthews & Mathieu 1992). In the case of an eccentric orbit, Hut (1981) has shown that the rotational angular velocity of a star will tend to synchronize with that of the orbital motion at periastron, a condition called pseudosynchronous rotation. With the periastron separation used as the semimajor

axis, a period of 8.78 days results. Our computed radii from Section 2.1 then produce pseudosynchronous velocities of 19.6 and 20.2 km s^{-1}. Both values are much smaller than our equatorial rotational velocities. Given the youth of the system, its moderate orbital period, and the fact that neither star has a significant outer convective envelope, it is not surprising that the rotational velocities of the components have not decreased to their pseudosynchronous values.

Gray & Garrison (1989), Gray et al. (2001), and others have classified the composite spectrum of δ Del as a peculiar early F star, and Reimers (1976) found that its two components have identical peculiar chemical compositions. Such findings are consistent with the computed equatorial rotational velocities of the two stars, which are both less than 120 km s^{-1}, the value below which A and early F stars generally have peculiar metal abundances (Abt & Morrell 1995).

5.2. Position on HR Diagram

With our measured radii and flux ratios from MIRC and PAVO data, we are able to plot the position of both components of δ Del on an HR diagram. We use MESA Isochrones and Stellar Tracks (MIST) models to plot isochrones and tracks for different stellar masses (Paxton et al. 2011, 2013, 2015; Choi et al. 2016; Dotter 2016). When compared to solar metallicity tracks, the track masses that match our luminosity and temperature determinations are not consistent with our best-fit masses of $1.78\,M_\odot$ and $1.62\,M_\odot$ from our orbit. However, the metallicities for δ Del listed on SIMBAD suggest that this system may be metal-poor. There is a spread in metallicity measurements from solar to metal-poor values, depending largely on the adopted value of the effective temperature. Reimers (1976) measure $[\text{Fe/H}] = -0.35$, whereas Cenarro et al. (2007) report $[\text{Fe/H}] = -0.30$. We find that a value of $[\text{Fe/H}] = -0.5$ gives solar tracks that are most consistent with our mass, luminosity, and temperature determinations. The position of each component of δ Del on an HR diagram, along with stellar tracks and isochrones, are shown for both low and solar metallicities in Figures 10 and 11. The mean $H\beta$ value, $b - y$, and $B - V$ colors listed in SIMBAD suggest a mean spectral class of about F0, which is what was found by Morgan & Abt (1972) and Gray & Garrison (1989). The best luminosity class estimates indicate that the average component for δ Del is evolved, consistent with our HR diagram results. Thus, the stars have evolved to late A- or
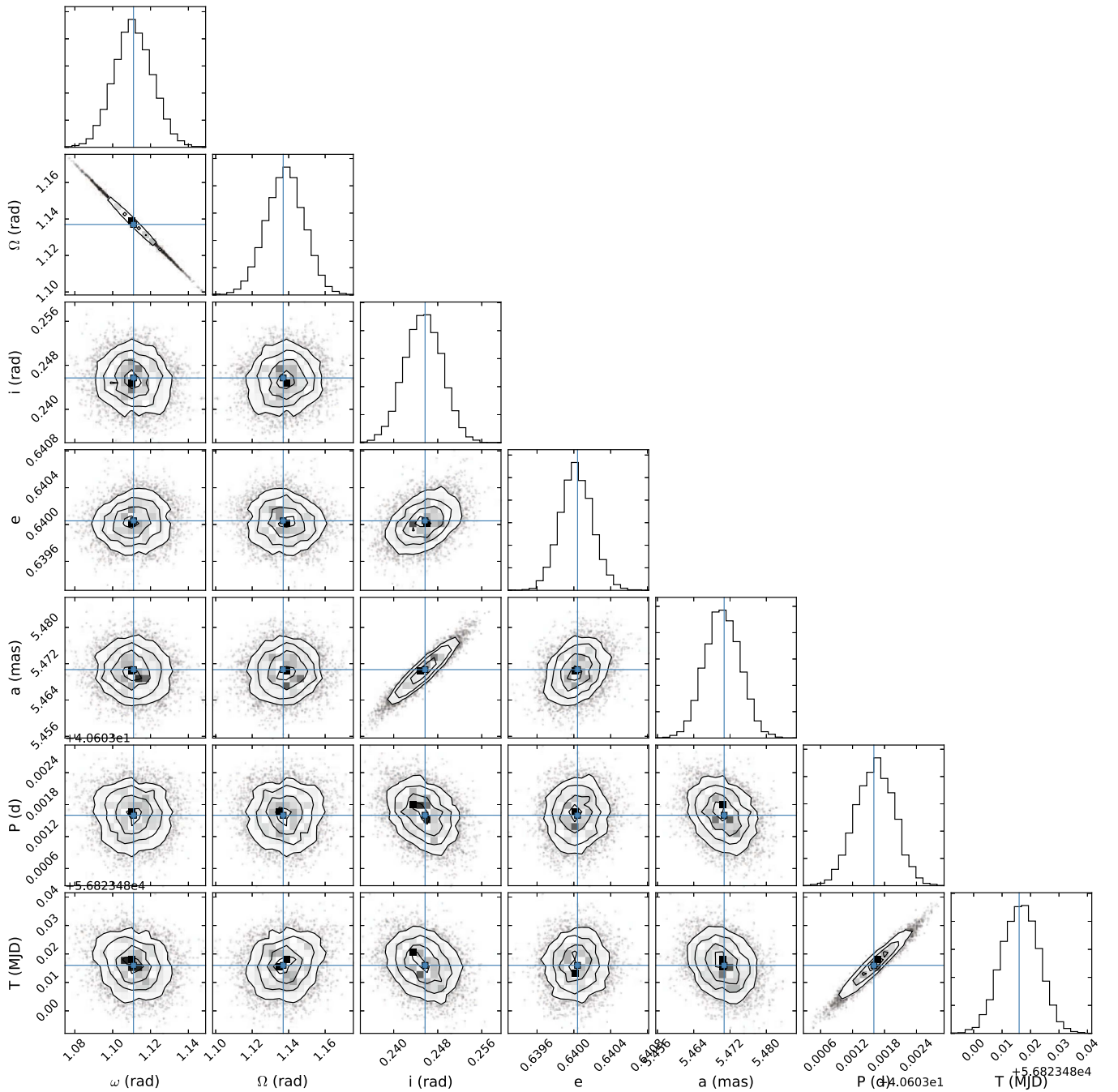
Figure 4. A corner plot of parameter distributions from the MCMC routine for astrometry data. Histograms display the number of times a given value was chosen as the best value for that element, and 2D plots show correlations between parameters. The crosshairs denote the best fit from least-squares fitting.

early F-type positions, and were most likely originally late A-type stars.

As can be seen from Figure 10, the individual masses determined from orbital fitting of RV and astrometry data are consistent with the measured radii and flux ratios only if one stellar component is more evolved than the other. Note that, although the error bars in Figure 10 seem to overlap, the mass ratio above unity measured from the spectroscopic orbit makes overlap impossible. The position of the lower-mass star on the HR diagram suggests an age >1.2 Gyr, while the age of the higher-mass star is just over 1 Gyr. This ∼200 Myr age difference is puzzling, as one would expect two stars of a close binary system to be the same age. Because the components of

δ Del are only separated at maximum RV separation, one possibility for this odd HR diagram placement is that there are systematic errors present in our RV results that affect the mass ratio. The properties of the two stars derived from inter-ferometry suggest that the mass ratio should be very close to unity, while our measured value from the spectroscopic orbit is ∼1.1. It is not clear in which direction possible systematics would change the semi-amplitudes—and hence, the mass ratio. The situation is further complicated by the pulsation of both components. Though we do not see any obvious systematics from our test described in Section 2.2, we nevertheless caution that systematic errors of the RV semi-amplitudes are a possible explanation for the odd positions of the components in the HR
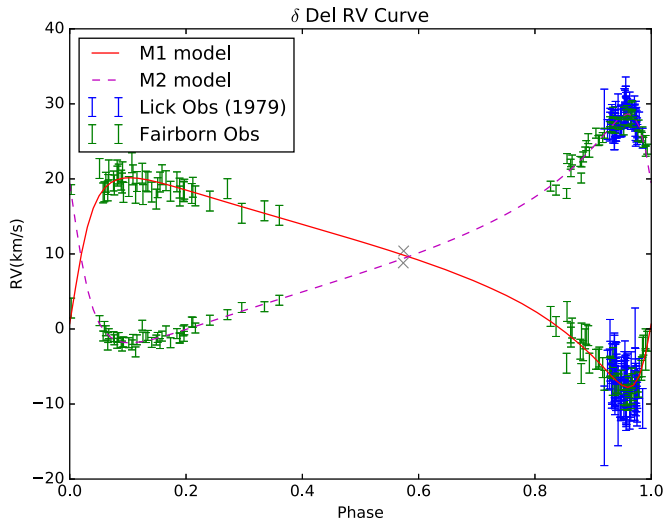
Figure 5. Double-lined radial velocities along with the best-fit model. The RV data combines 97 data points from Fairborn Observatory with 87 unpublished RVs from Lick Observatory (Duncan & Preston 1979). The two gray marks just before phase 0.6 are velocities obtained from single-lined spectra. These points are not included in the best fit, but the measurements do help support our system velocity and mass ratio values.
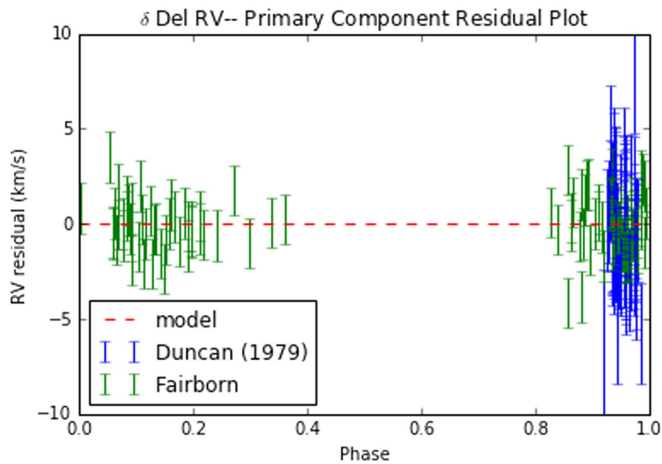
Figure 6. Residual plot of the primary component of δ Del from the best-fit RV orbit.

Figure 7. Residual plot of the secondary component of δ Del from the best-fit RV orbit.

diagram. The two single-lined RVs that we measure when both components are at their center-of-mass velocity add further support that our value for system velocity is correct. This strengthens the claim of the mass ratio from the RV orbit, though we reiterate that these two velocity measurements are of low precision due to δ Scuti pulsations and different rotational velocities of the components that will not, in general, average out.

Assuming that there are no systematic errors present in the mass ratio, we can think of four possible explanations that would resolve the age difference problem in the HR diagram: (1) δ Scuti stars age differently than normal stars on the immediate post-main-sequence branch, (2) stellar evolution models are not accurate on the subgiant branch, (3) early interaction with a third component caused a difference in evolution rates, or (4) the age difference in the components of δ Del is a result of a merger event for the inner stars of an initially triple system.

Theoretically, δ Scuti stars are expected to evolve as normal stars on the main sequence and immediate post-main sequence (e.g., Baglin et al. 1973; Breger 1979, 1980). However, as pointed out by Petersen & Christensen-Dalsgaard (1996), there is very little observational proof of this hypothesis. Recently, Niu et al. (2017) used photometric and spectroscopic data on the δ Scuti variable AE Ursae Majoris to provide such evidence that δ Scuti variables do, in fact, evolve as normal stars on the immediate post-main sequence. However, one observation may not be sufficient for making this claim about all δ Scuti variables. A potential cause of abnormal aging among δ Scuti variables is the non-solar metal abundances present at the photosphere (e.g., Guzik et al. 1998). As pointed out by North et al. (1997), metallicity determination of δ Scuti variables may only be confined to the superficial layers of these stars and not reflect an internal metal distribution. Thus, mass determination via standard solar-scaled models may be invalid for these stars. Tsvetkov (1990) compared three different types of mass determinations for 89 δ Scuti variables. Although the mass determined from the evolutionary state on the HR diagram was consistent for most of their sample, the different methods of mass determination produced inconsistent results for nine of their stars. The mass determination via the HR diagram differed by a factor of 2–5 between other methods. Hence, the HR diagram may not be reliable for mass determination for δ Scuti variables. North et al. (1997) also note that there is no one-to-one relation between mass and position on an HR diagram at the end of the core-hydrogen exhaustion phase. We find that δ Del lies right around this phase in stellar evolution, which may account for the discrepancies between mass prediction from the MIST stellar model and from the combined spectroscopic and visual orbit.

Close binary star evolution is generally a complex topic, where the closest systems often involve formation scenarios in which the systems interact with a tertiary companion (Tokovinin 2004), and interaction with the circumstellar and circumbinary disks means that stars can be born with a variety of initial rotational velocities. Differential rotational velocities change interior mixing and can cause a difference in evolutionary rates. Additionally, interaction (such as accretion of He-rich material) with a now-ejected, initially higher-mass companion could also cause a difference in the evolutionary states between the two components.
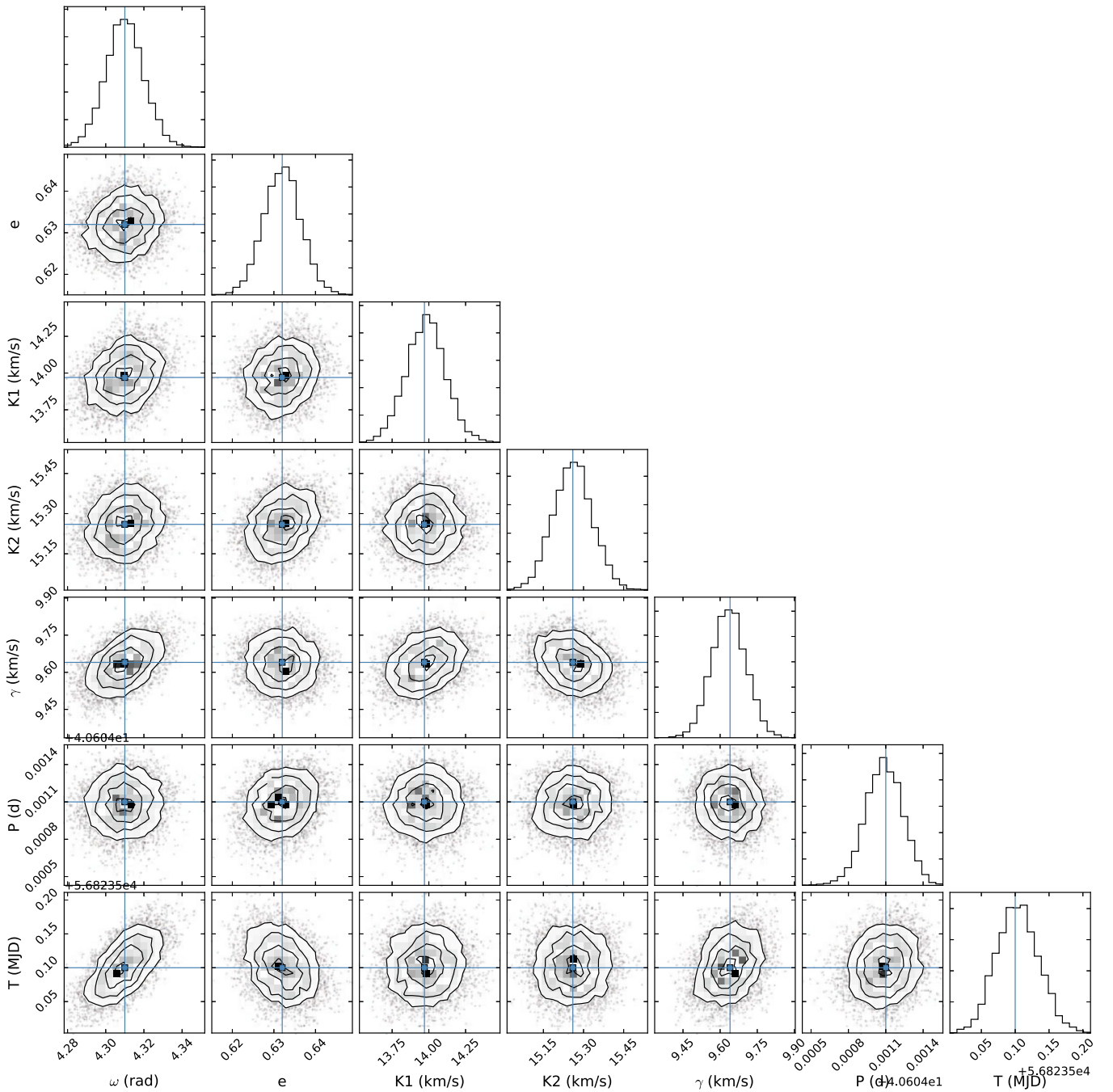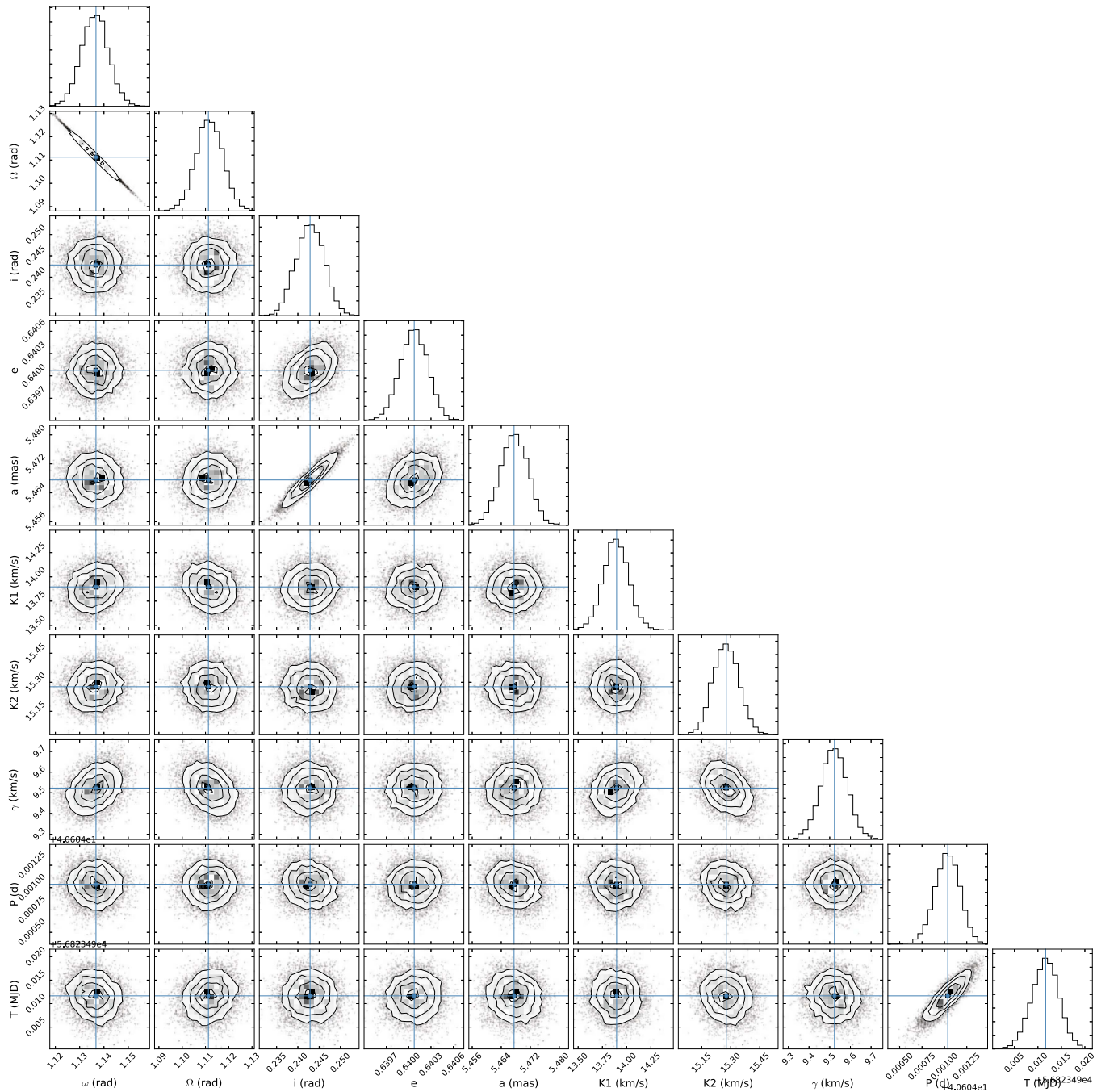
Figure 8. A corner plot of parameter distributions from the MCMC routine for RV data. Histograms display the number of times a given value was chosen as the best value for that element, and 2D plots show correlations between parameters. The crosshairs denote the best fit from least-squares fitting.

If the MIST models do, in fact, correctly describe these components, then the low-mass component must have an age of just over 1.2 Gyr, while the high-mass component has an age of just over 1.0 Gyr. A possible way to account for this age difference is to assume that one of the stars is the result of a merger event. An inner binary of an initially triple system would have had to merge within ~200 Myr. The result of the merger would be a single star (the more massive component) that then evolved normally within the now-binary system. The merger hypothesis has been proposed before, to explain the existence of peculiar stars, and merger timescales of 100–500 Myr are theoretically possible (e.g., Andrievsky 1997; de Mink et al. 2014). However, there are two major problems

with one component of δ Del being the result of a merger event: (1) merger products are likely to have abnormal rotation rates, and (2) merger products are not likely to have a non-affected nearby main-sequence companion (de Mink et al. 2014). We know that δ Del has both a relatively slow rotation rate and a very nearby companion. It is beyond the scope of this paper to determine whether or not it is truly possible for one component of this close binary system to be the result of an early merger event. Although it seems to be an unlikely scenario, if the stellar evolution models are correct for this binary, then an early interaction with a tertiary component is the only possibility we can think of to resolve the age discrepancy seen in the HR diagram.

Figure 9. A corner plot of parameter distributions from the MCMC routine for combined astrometry and RV data. Histograms display the number of times a given value was chosen as the best value for that element, and 2D plots show correlations between parameters. The crosshairs denote the best fit from least-squares fitting.

6. Toward Astrometric Detection of Exoplanets

From the ground, long-baseline interferometry is a promising method for using differential astrometry to detect exoplanets. The astrometric detection method favors planets farther from the host star, unlike RV or transit surveys. Moreover, interferometric binary observations favor hot (A- and B-type) binary stars, which are difficult to probe via RV surveys because of weak and broad spectral lines. Thus, developing the capability to detect exoplanets with the MIRC instrument can probe a region that is not well-explored by other detection methods. The recent PHASES project monitored binary stars with the Palomar Testbed Interferometer to obtain precise differential astrometric orbits, and detected six candidate

substellar objects orbiting single stars of a binary system (Muterspaugh et al. 2010). Unfortunately this project was halted due to the closure of the Palomar Testbed Interferometer in 2009. In this section, we demonstrate that the MIRC instrument at CHARA is capable of achieving the precision necessary for astrometric detection of exoplanets. The precision needed to detect the wobble of a star at δ Del's distance from a Jupiter-mass planet within a few au is on the order of 10 μas. With our δ Del orbit, MIRC has achieved this precision in differential position for one star in a binary system with 10 minute observations. Thus, if there were a large planet around one component of δ Del, it would be possible to detect as residuals on our astrometric orbit. Claiming a detection is

Table 11
Best-fit Physical Elements from Combining RV and Astrometry Data

Physical Element	Best Value
Parallax, π (mas)	15.72 ± 0.22 (± 0.04)[a]
Distance, d (pc)	63.61 ± 0.89 (± 0.16)[a]
Semimajor axis, a (au)	0.348 ± 0.005
M_1/M_2	1.100 ± 0.012
M_1 ($M_\odot$)	1.78 ± 0.07
M_2 ($M_\odot$)	1.62 ± 0.07

Note.
[a] Systematic error in parentheses.

not simple, as it involves adding seven planet orbital parameters to the seven-parameter binary model. Adding free parameters to a model may lower the χ^2 of a fit, but this does not necessarily make it a "better" model. A detection criterion often used for claiming RV planet detections is the Bayesian Information Criteria (BIC) value (e.g., Motalebi et al. 2015; Sato et al. 2015; Feng et al. 2016). The BIC is computed by

$$\text{BIC} = -2\ln\mathcal{L} + k\ln n, \qquad (5)$$

where k is the number of free parameters, n is the number of data points, and $\mathcal{L}$ is the likelihood function. For our models, $-2\ln\mathcal{L} = \chi^2$. When comparing two models, the one with a lower BIC value is selected as being a better fit to the data.

We do not detect a planet around either component of δ Del, which is unsurprising because the binary separation is $\sim$0.3 au. Still, we can use the precision of this orbit to test planet detection limits around δ Del and gain insight as to the types of planets we can detect when extending this precision to wider binary systems. To compute detection limits, we add simulated planet wobbles to our observations, then fit the resulting data with a binary fit and a binary+planet fit. Note that we are testing for planets around individual stars of a binary system. While it is possible that a circumbinary planet exists around δ Del, our differential astrometric data is not sensitive to these types of orbits. We also emphasize that, in this study, we are only testing which planets show statistically significant detection signals with our measurement precision. Sophisticated fitting routines and many epochs of observations will be needed to recover the full orbit of real planets. Though fitting to 14 free parameters is a formidable challenge, in reality we will target systems where the seven binary parameters are known quite well. Thus, only the seven planet orbital elements will truly be free parameters. Future work of our group will include developing such fitting routines, building off the work of recent studies that have tackled this challenge (e.g., Perryman et al. 2014; Sozzetti et al. 2014; Ranalli et al. 2017).

The position of one star plotted relative to the companion is a sum of the position due to the binary orbit and the perturbation from the planet. Relative to a star at the origin, we can calculate the position vector $[x_s(t), y_s(t)]$ of one companion. We can also calculate the perturbation on a star due to an orbiting planet. Using the planet orbital elements, the position vector of the star from the planet is $[x_p(t), y_p(t)]$. The final astrometric position of a star with a binary companion and orbiting planet is then a sum of the two vectors

$$[x(t), y(t)] = [x_s(t), y_s(t)] + \frac{[x_p(t), y_p(t)]}{1 + M_s/M_p}, \qquad (6)$$
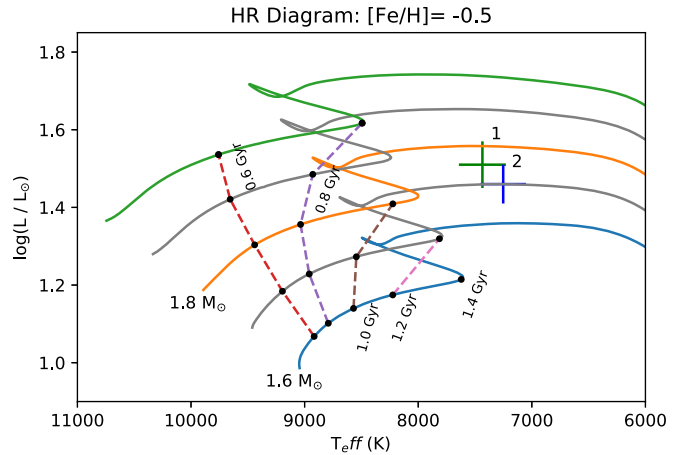
Figure 10. Position of both components of δ Del on an HR diagram for the low-metallicity case. MIST models are used to compute the plotted stellar tracks (solid lines) and isochrones (dashed lines). The luminosity and temperature values are consistent with our determined masses, if component 2 is more evolved than component 1.
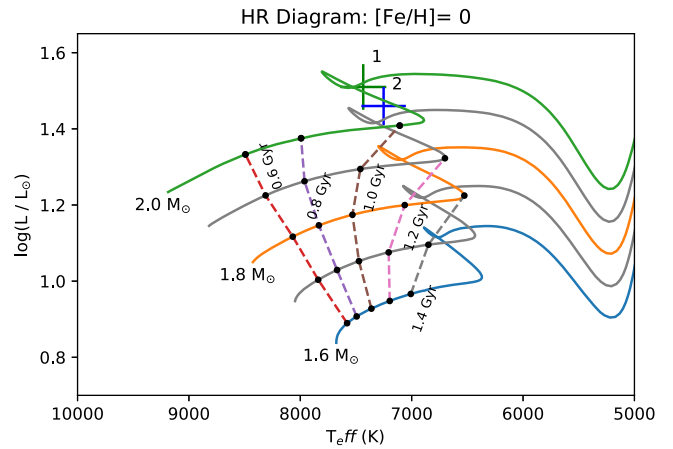
Figure 11. Position of both components of δ Del on an HR diagram for the solar metallicity case. MIST models are used to compute the plotted stellar tracks (solid lines) and isochrones (dashed lines). The masses predicted from the HR diagram in this case are not consistent with those determined from our orbit.

where M_s is the mass of the star and M_p is the planet mass. The planet vector is shortened because we are only seeing the reflex motion of the star due to the presence of the planet.

To test planet detection limits around δ Del, we simulate 10 planets with 0 eccentricity and random values for ω, Ω, i, and T_0 at each point on a grid with semimajor axes varying from 0.01 to 3 au and masses from 0.01 to $10\,M_J$. We record the percentage of the planets we successfully recover at each grid point. The planet perturbation at the time of data collection is added to each real data point of our δ Del orbit. For each simulated planet, we perform a binary fit (seven parameters) and a binary+planet fit (14 parameters), then compare the BIC values. We use the known binary and simulated planet parameters as initial guesses for a least-squares fit to compute χ^2 for the binary and binary+planet model. The model including a planet in the binary system is considered better if it has a lower BIC value and $\Delta\text{BIC} > 5$ between the models (Liddle 2007). We consider true detections to be those in which the recovered planet mass and semimajor axis are within 30%
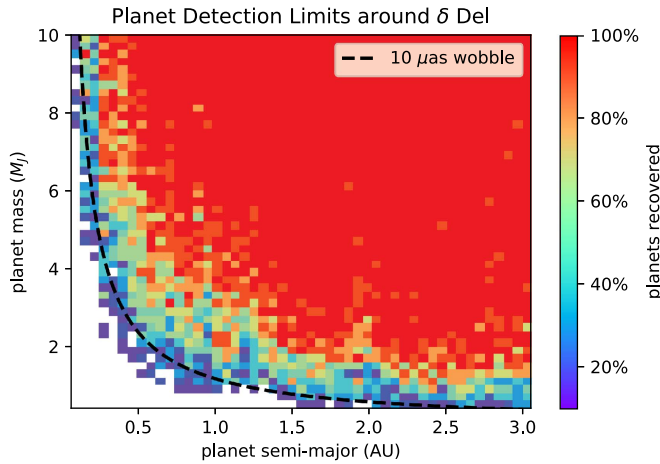
Figure 12. Planet detection limits around δ Del are computed by simulating the wobble from a planet at each point on a mass, semimajor grid. A candidate detection is made based on the BIC criterion. If the best-fit planet mass and semimajor axis are within 30% of the actual input values then we classify it as a true detection. For each mass, semimajor grid point we simulate 10 planets with random orbital elements and record the percentage of the time the planet is recovered. The dashed curve denotes the points on the grid where a planet would impart a 10 micro-arcsecond wobble on the star.

of the true input values of the simulated planet. Figure 12 displays our planet detection limits around a binary star with the observational precision of δ Del. Our detection limits suggest that, with MIRC, we are able to recover most planets $>2\,M_J$ at orbits >0.75 au around single components of intermediate-mass close-binary systems.

The *Gaia* mission will also use the astrometry method for discovering giant exoplanets. While *Gaia* is expected to be extremely successful in recovering massive planets around low-mass stars, companions with mass $M_P < 10\,M_J$ around A- and B-type stars will likely remain undetectable by *Gaia*. A common criterion for detection of an undiscovered exoplanet with *Gaia* is

$$ \mathrm{S/N} = a\left(\frac{\sigma_\Lambda}{\sqrt{N}}\right)^{-1} > 20, \qquad (7) $$

where σ_Λ is the single-epoch measurement error, a is the semimajor axis of the detected orbit, and N is the number of observations (Sahlmann et al. 2016). Using the criteria for a discovery with $\sigma_\Lambda = 50\,\mu$as and $N = 70$ measurements over 5 years, a $1\,M_J$ planet on a 3 au orbit around an A-type star of $2\,M_\odot$ could be detected out to 10 pc. Since there are just 4 A-type stars within 10 pc, Jupiter-mass planet discoveries around massive stars are expected to be rare with *Gaia*. A $10\,M_J$ planet on a 3 au orbit around an A-type star is detectable out to 100 pc, where there are over 400 A-type stars available for study (De Rosa et al. 2014). Thus, companions $\sim10\,M_J$ and greater around A-type stars should be detectable with *Gaia*. With better single-epoch measurements, we plan to search for Jupiter-mass planets on orbits <5 au around A- and B-type stars, which will complement the more massive companions discovered by *Gaia*.

7. Summary

Obtaining both spectroscopic and visual orbits of binary stars allows one to measure the full 3D orbit, masses, and parallax of
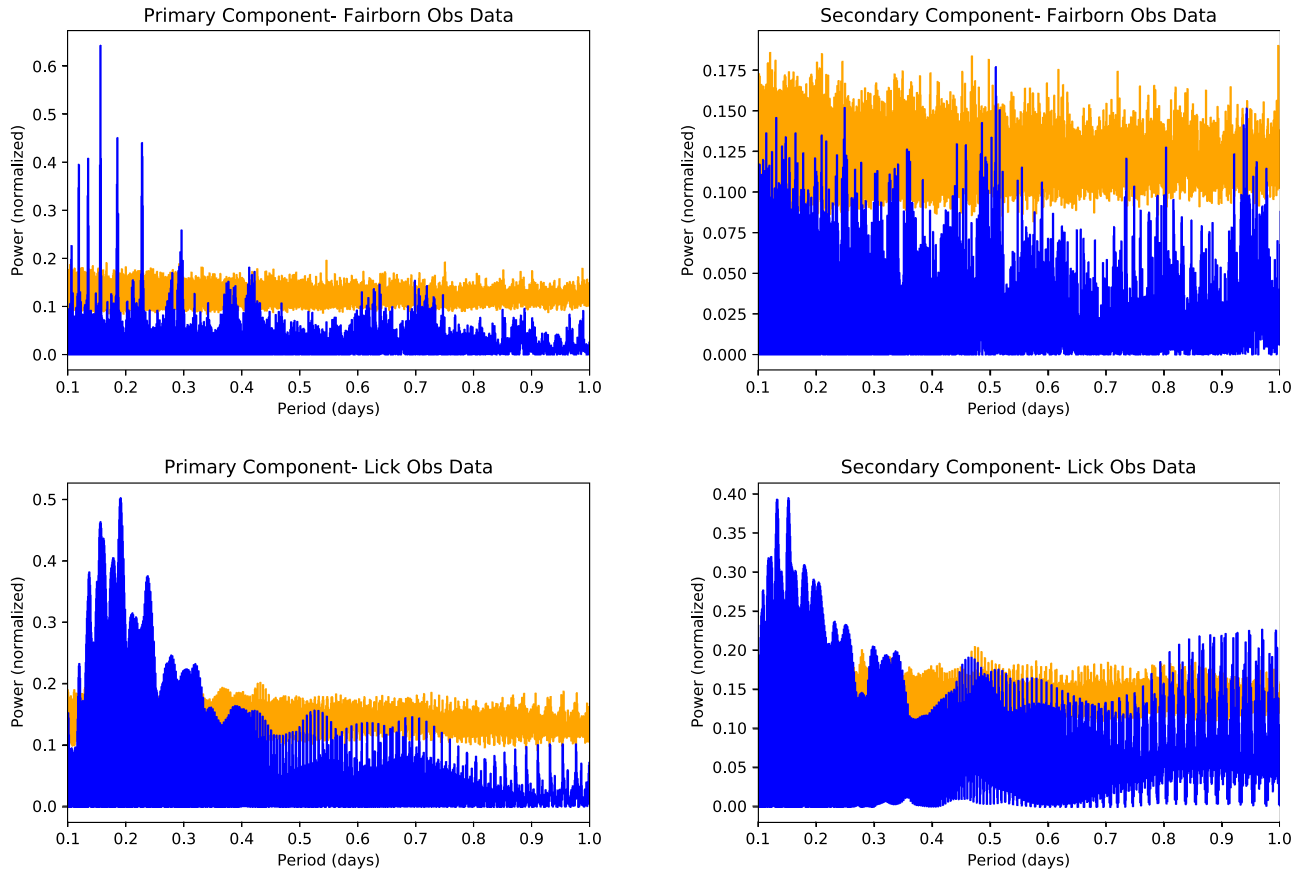
the system. This information is crucial for testing models of stellar evolution. In this work, we have obtained a highly precise visual orbit with >2 years of data from the MIRC instrument on the CHARA long-baseline interferometer. We also use 97 new spectra from Fairborn Observatory along with 87 unpublished spectra obtained at Lick Observatory by Duncan & Preston (1979) to obtain a double-lined spectroscopic binary orbit. In our full binary analysis of δ Del, we determine component masses of $1.78 \pm 0.07\,M_\odot$ and $1.62 \pm 0.07\,M_\odot$. We measure a distance of 63.61 ± 0.89 (±0.16 systematic error) pc, which differs from the revised *Hipparcos* value of 68.45 ± 0.94 pc.

We find that the evolutionary state of δ Del is puzzling. Combining our H-band MIRC observations with R-band data from the PAVO instrument on CHARA, we are able to determine individual magnitudes and temperatures for each component. A metallicity of $[\mathrm{Fe/H}] = -0.5$ is required to match our mass determination to MIST stellar models. The position on the HR diagram, however, implies that one component is more evolved than the other by ~200 Myr. We propose four possibilities that may explain this seemingly impossible evolutionary state: (1) stellar models are incorrect on the subgiant branch, (2) δ Scuti variables evolve differently than normal stars just after the main sequence, (3) interactions with a now-ejected tertiary companion created different mixing processes for each component, or (4) the more massive component of δ Del is the result of a merger event at an age of ~200 Myr, which then evolved as a normal star.

Because of the high precision of our visual orbit of δ Del, we calculate exoplanet detection limits around one of the two stars of this binary system after accounting for the orbital motion of the companion. With the MIRC instrument, we have maintained $<10\,\mu$as precision on differential position over >2 years. This is the precision needed to detect Jupiter-mass planets at orbits up to a few au. Though the presence of a planet around a component of δ Del is unlikely because of the extremely close binary separation, we have shown that, if this precision can be extended to wider binaries, MIRC is within reach of detecting planets $>2\,M_J$ at orbits >0.75 au. Developing this capability will allow us to search for exoplanets in regimes that are difficult to probe with RV and transit surveys, such as around hot binary stars. Our group is starting project ARMADA (ARrangement for Micro-Arcsecond Differential Astrometry), which will use MIRC at the CHARA array to target hot binary stars with the goal of detecting massive exoplanets on orbits up to a few au around intermediate-mass stars.

---

[18] Available at http://www.jmmc.fr/searchcal_page.htm.

Figure 13. After subtracting out the best-fit RV orbit, we search for additional periodicity in the data due to δ Scuti pulsations. We detect significant peaks in the primary component of the Fairborn data and both components of the Lick data. The orange background signal depicts peaks of three-sigma significance determined by bootstrapping. The peaks in the secondary component of the Fairborn data are not highly significant.

Appendix
δ Scuti Pulsations

Because of short period variations in their RV curves, both components of δ Del have been previously classified as δ Scuti variables with periods of 0.158 ± 0.006 days for the primary (more massive) component and 0.134 ± 0.015 days for the secondary (Duncan & Preston 1979). However, this previous analysis of the 1979 Lick Observatory data also concluded that there are multiple periodicities in the δ Scuti pulsations. Hence, fitting the pulsations to a single sinusoid with the peak period does not capture the true nature of these variations. More evenly sampled data at all epochs is likely needed to thoroughly model these pulsations. Nevertheless, we describe a "first-order" correction of these pulsations in order to improve the overall RV fit.

We first carry out a least-squares fit to all of the RV data from Fairborn and Lick observatories, and we subtract out the resulting best-fit RV for each data point. We then search for additional periodic signals in the residuals by generating a Lomb–Scargle periodogram with the built-in function from the *astropy* package (Astropy Collaboration et al. 2013). A single sinusoid is fit to the residual data with a period determined from the highest peak of the periodogram. The significance of a peak is determined by estimating the false-alarm probability (FAP) using the bootstrap method described in (Murdoch et al. 1993).

In the Fairborn Obs data, we find a significant peak in the primary at 0.157 days. The secondary component, however, shows no significant peaks in the Fairborn data. The strongest peak in the periodogram has a FAP of ∼0.91, suggesting that it is not a true signal. Thus, we do not model any pulsations in this component for the Fairborn data. We detect significant peaks in both components of the 1979 Lick Observatory data, though the periodograms show peaks for many different periods. For the secondary component in the Lick Observatory data, we model the pulsations with the first peak at 0.1323 days, within the error bars of the 1979 analysis. Because there is also a peak at 0.157 days for the primary component in the Lick data, we again use this period to model the pulsations of the primary. We subtract the δ Scuti pulsations out of the RV data, separately for the Fairborn and Lick Observatory velocities, and re-fit the resulting data with our RV model. Our reduced χ^2 value for the RV fit decreases from 3.5 to 1.8 after subtracting out the pulsations. The periodograms for each
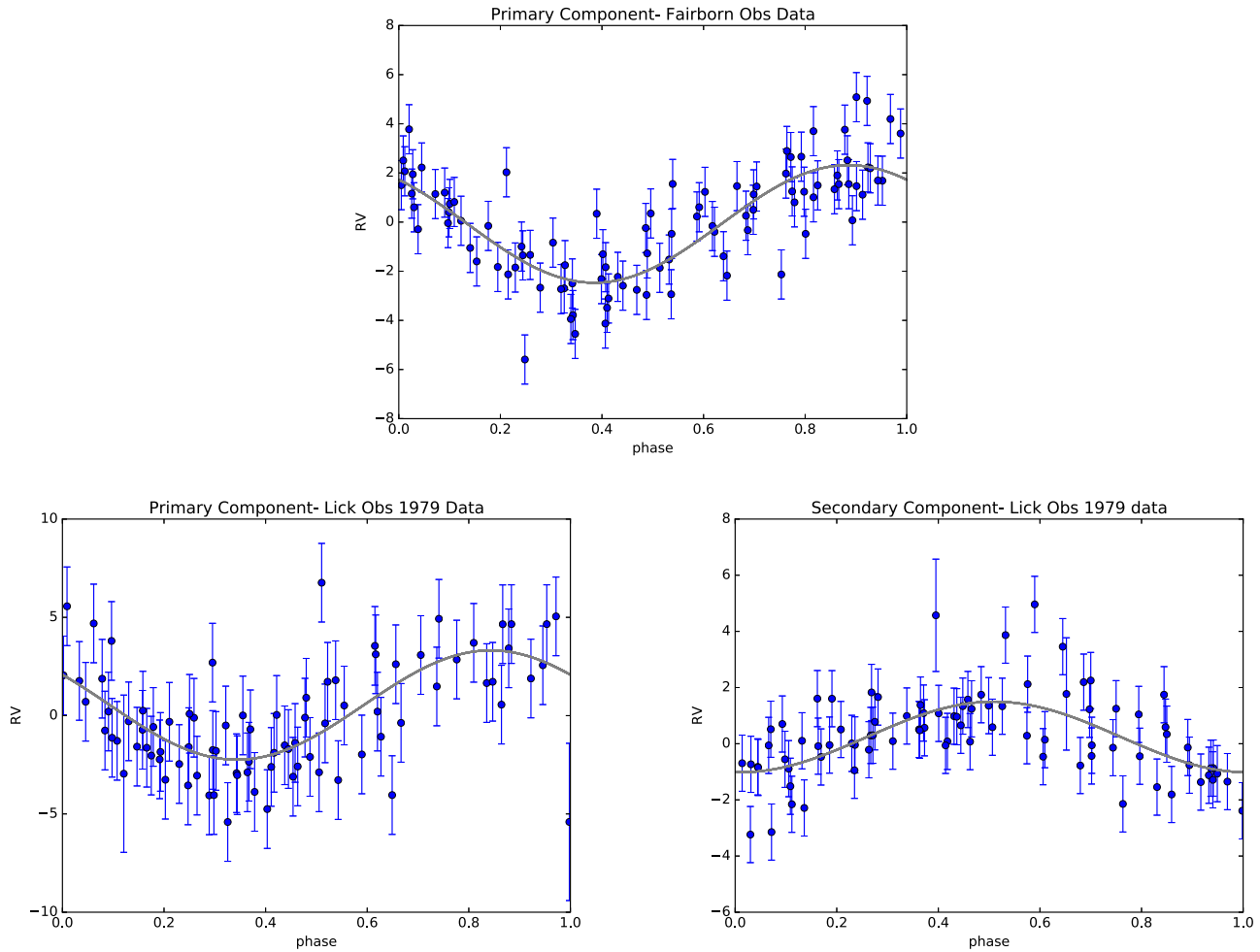
Figure 14. δ Scuti pulsations in the residuals for the Fairborn and Lick RV data after the best-fit orbit is subtracted out. The primary component of both data sets has a period of 0.157 days. The secondary in the Lick data has a period of 0.132 days. We detect no significant period signal for the secondary in the Fairborn Observatory data. Figures are phase-folded with $T_0 = 56823.6$.

data set are shown in Figure 13. Figure 14 shows the δ Scuti pulsations of the primary in the Fairborn data and both components in the Lick data.

ORCID iDs

Tyler Gardner ⓘ https://orcid.org/0000-0002-3003-3183
John D. Monnier ⓘ https://orcid.org/0000-0002-3380-3307
Francis C. Fekel ⓘ https://orcid.org/0000-0002-9413-3896
Timothy R. White ⓘ https://orcid.org/0000-0002-6980-3392
Michael Ireland ⓘ https://orcid.org/0000-0002-6194-043X
Fred C. Adams ⓘ https://orcid.org/0000-0002-8167-1767
Fabien Baron ⓘ https://orcid.org/0000-0002-5074-1128
Daniel Huber ⓘ https://orcid.org/0000-0003-4894-9779
Stefan Kraus ⓘ https://orcid.org/0000-0001-6017-8773
Rachael M. Roettenbacher ⓘ https://orcid.org/0000-0002-9288-3482
Gail Schaefer ⓘ https://orcid.org/0000-0001-5415-9189
Samuel J. Swihart ⓘ https://orcid.org/0000-0003-1699-8867

References

Abt, H. A., & Morrell, N. I. 1995, ApJS, 99, 135
Andrievsky, S. M. 1997, A&A, 321, 838
Astropy Collaboration, Robitaille, T. P., Tollerud, E. J., et al. 2013, A&A, 558, A33
Baglin, A., Breger, M., Chevalier, C., et al. 1973, A&A, 23, 221
Barnes, T. G., Evans, D. S., & Moffett, T. J. 1978, MNRAS, 183, 285
Bonneau, D., Millour, F., & Meilland, A. 2014, in EAS Publications Ser. (Vol. 69; Les Ulis: EDP Sciences), 335
Breger, M. 1979, PASP, 91, 5
Breger, M. 1980, SSRv, 27, 361
Casertano, S., Lattanzi, M. G., Sozzetti, A., et al. 2008, A&A, 482, 699
Castelli, F., & Kurucz, R. L. 2004, arXiv:astro-ph/0405087
Cenarro, A. J., Peletier, R. F., Sánchez-Blázquez, P., et al. 2007, MNRAS, 374, 664
Chelli, A., Duvert, G., Bourgès, L., et al. 2016, A&A, 589, A112
Choi, J., Dotter, A., Conroy, C., et al. 2016, ApJ, 823, 102
Cutri, R. M., Skrutskie, M. F., van Dyk, S., et al. 2003, yCat, 2246
de Mink, S. E., Sana, H., Langer, N., Izzard, R. G., & Schneider, F. R. N. 2014, ApJ, 782, 7
De Rosa, R. J., Patience, J., Wilson, P. A., et al. 2014, MNRAS, 437, 1216
Dotter, A. 2016, ApJS, 222, 8
Duncan, D. K., & Preston, G. W. 1979, BAAS, 11, 728
Eaton, J. A., & Williamson, M. H. 2007, PASP, 119, 886
Eggen, O. J. 1956, PASP, 68, 541
Fekel, F. C., & Griffin, R. F. 2011, Obs, 131, 283
Fekel, F. C., Rajabi, S., Muterspaugh, M. W., & Williamson, M. H. 2013, AJ, 145, 111
Fekel, F. C., Tomkin, J., & Williamson, M. H. 2009, AJ, 137, 3900
Feng, F., Tuomi, M., Jones, H. R. A., Butler, R. P., & Vogt, S. 2016, MNRAS, 461, 2440
Foreman-Mackey, D., Hogg, D. W., Lang, D., & Goodman, J. 2013, PASP, 125, 306

Gelman, A., & Rubin, D. B. 1992, StaSc, 7, 457
Gray, R. O., & Garrison, R. F. 1989, ApJS, 69, 301
Gray, R. O., Napier, M. G., & Winkler, L. I. 2001, AJ, 121, 2148
Guzik, J. A., Templeton, M. R., & Bradley, P. A. 1998, in ASP Conf. Ser. 135, A Half Century of Stellar Pulsation Interpretation, ed. P. A. Bradley & J. A. Guzik (San Francisco, CA: ASP), 470
Hut, P. 1981, A&A, 99, 126
Ireland, M. J., Mérand, A., ten Brummelaar, T. A., et al. 2008, Proc. SPIE, 7013, 701324
Kervella, P., Thévenin, F., Di Folco, E., & Ségransan, D. 2004, A&A, 426, 297
Liddle, A. R. 2007, MNRAS, 377, L74
Lucy, L. B. 2014, A&A, 563, A126
Matthews, L. D., & Mathieu, R. D. 1992, in ASP Conf. Ser. 32, IAU Coll. 135: Complementary Approaches to Double and Multiple Star Research, ed. H. A. McAlister & W. I. Hartkopf (San Francisco, CA: ASP), 244
Monnier, J. D., Che, X., Zhao, M., et al. 2012, ApJL, 761, L3
Monnier, J. D., Pedretti, E., Thureau, N., et al. 2006, Proc. SPIE, 6268, 62681P
Morel, M., & Magnenat, P. 1978, A&AS, 34, 477
Morgan, W. W., & Abt, H. A. 1972, AJ, 77, 35
Motalebi, F., Udry, S., Gillon, M., et al. 2015, A&A, 584, A72
Mourard, D., Monnier, J. D., Meilland, A., et al. 2015, A&A, 577, A51
Murdoch, K. A., Hearnshaw, J. B., & Clark, M. 1993, ApJ, 413, 349
Muterspaugh, M. W., Lane, B. F., Kulkarni, S. R., et al. 2010, AJ, 140, 1657
Newville, M., Stensitzki, T., Allen, D. B., & Ingargiola, A. 2014, LMFIT: Non-Linear Least-Square Minimization and Curve-Fitting for Python, Zenodo, doi:10.5281/zenodo.11813
Niu, J.-S., Fu, J.-N., Li, Y., et al. 2017, MNRAS, 467, 3122
North, P., Jaschek, C., & Egret, D. 1997, in ESA Special Publication 402, Hipparcos—Venice '97, ed. R. M. Bonnet et al. (Paris: ESA), 367

Pauls, T. A., Young, J. S., Cotton, W. D., & Monnier, J. D. 2005, PASP, 117, 1255
Paxton, B., Bildsten, L., Dotter, A., et al. 2011, ApJS, 192, 3
Paxton, B., Cantiello, M., Arras, P., et al. 2013, ApJS, 208, 4
Paxton, B., Marchant, P., Schwab, J., et al. 2015, ApJS, 220, 15
Perryman, M., Hartman, J., Bakos, G. Á., & Lindegren, L. 2014, ApJ, 797, 14
Perryman, M. A. C., Lindegren, L., Kovalevsky, J., et al. 1997, A&A, 323, L49
Petersen, J. O., & Christensen-Dalsgaard, J. 1996, A&A, 312, 463
Ranalli, P., Hobbs, D., & Lindegren, L. 2017, arXiv:1704.02493
Reimers, D. 1976, A&A, 53, 377
Sahlmann, J., Lazorenko, P. F., Ségransan, D., et al. 2014, MmSAI, 85, 674
Sahlmann, J., Martín-Fleitas, J., Mora, A., et al. 2016, Proc. SPIE, 9904, 99042E
Sandberg Lacy, C. H., & Fekel, F. C. 2011, AJ, 142, 185
Sato, B., Hirano, T., Omiya, M., et al. 2015, ApJ, 802, 57
Scarfe, C. D. 2010, Obs, 130, 214
Sozzetti, A., Giacobbe, P., Lattanzi, M. G., et al. 2014, MNRAS, 437, 497
Struve, O., Sahade, J., & Zebergs, V. 1957, ApJ, 125, 692
Tassoul, J.-L. 1987, ApJ, 322, 856
Tassoul, J.-L., & Tassoul, M. 1992, ApJ, 395, 259
ten Brummelaar, T. A., McAlister, H. A., Ridgway, S. T., et al. 2005, ApJ, 628, 453
Tokovinin, A. 2004, RMxAA, 21, 7
Torres, G., Andersen, J., & Giménez, A. 2010, A&ARv, 18, 67
Tsvetkov, T. G. 1990, Ap&SS, 173, 1
van Leeuwen, F. 2007, A&A, 474, 653
White, T. R., Huber, D., Maestro, V., et al. 2013, MNRAS, 433, 1262
Wright, J. T., & Howard, A. W. 2009, ApJS, 182, 205
Zahn, J.-P. 1977, A&A, 57, 383